# Electromechanical characterization of carbon nanotubes grown on carbon fiber

Steven T. Patton, Qiuhong Zhang, Liangti Qu, Liming Dai, Andrey A. Voevodin et al.

## Related Articles

Nonlocal buckling behavior of bonded double-nanoplate-systems
J. Appl. Phys. 110, 084316 (2011)

Size-affected shear-band speed in bulk metallic glasses
Appl. Phys. Lett. 99, 171904 (2011)

The elastic properties of Mn3(Cu1xGex)N compounds
AIP Advances 1, 042125 (2011)

Uniaxial tension-induced breaking in the gold nanowire with the influence of defects and temperatures
J. Appl. Phys. 110, 084307 (2011)

Slippage toughness measurement of soft interface between stiff thin films and elastomeric substrate
Rev. Sci. Instrum. 82, 104704 (2011)

## Additional information on J. Appl. Phys.

Journal Homepage: http://jap.aip.org/

Journal Information: http://jap.aip.org/about/about_the_journal

Top downloads: http://jap.aip.org/features/most_downloaded

Information for Authors: http://jap.aip.org/authors

# Electromechanical characterization of carbon nanotubes grown on carbon fiber

Steven T. Patton,[1,2,a)] Qiuhong Zhang,[1,2] Liangti Qu,[2] Liming Dai,[2] Andrey A. Voevodin,[1] and Jeff Baur[1]

[1]*Materials and Manufacturing Directorate, Air Force Research Laboratory, Wright-Patterson Air Force Base, Ohio 45433-7750, USA*
[2]*University of Dayton Research Institute, Dayton, Ohio 45469-0168, USA*

Mechanical and electrical properties of carbon fiber (CF) and vertically aligned carbon nanotubes (CNTs) have been thoroughly investigated in previous studies. Growth of radially aligned CNTs on silicon oxide ($SiO_2$) coated CF has recently been accomplished resulting in multiscale composite fiber ($CNT/SiO_2/CF$). $CNT/SiO_2/CF$ offers promise as stress and strain sensors in CF reinforced composite materials. However, to date there have been no investigations of the electromechanical properties of $CNT/SiO_2/CF$ that would facilitate their usage as sensors in composite materials, which is the focus of this research. This study investigates fundamental mechanical and electrical properties of CF, $SiO_2/CF$ ($SiO_2$ coated CF), and $CNT/SiO_2/CF$ during localized transverse compression at low loads ($\mu$N to mN) and small displacements (nm to a few $\mu$ms). Force, strain, stiffness, and electrical resistance were monitored simultaneously during compression experiments. For CF, resistance decreased sharply upon compressive loading with hysteresis in both force and resistance being observed at low strain. For $SiO_2/CF$, high resistance and negligible electrical conduction occurred, and the force-displacement curve was linear. $CNT/SiO_2/CF$ stiffness increased as force and strain increased and became comparable to that of CF at high strain ($\sim$30%). Hysteresis in both force-displacement and resistance-displacement curves was observed with $CNT/SiO_2/CF$, but was more evident as maximum strain increased and did not depend on strain rate. Force was higher and resistance was lower during compression as compared to decompression. Hysteretic energy loss is associated with internal friction between entangled CNTs. Van der Waals force between deformed and entangled CNTs hindered disentanglement, which reduced the number of electrical current paths and increased resistance during decompression. The results of this study provide new understanding of the mechanical and electrical behavior of $CNT/SiO_2/CF$ that will facilitate usage as stress and strain sensors in both stand-alone and composite materials applications. © *2009 American Institute of Physics.* [doi:10.1063/1.3253747]

## I. INTRODUCTION

Mechanical and electrical properties of carbon fibers (CFs) and vertically aligned carbon nanotubes (CNTs) have been thoroughly investigated in previous studies. CNT coated CF (CNT/CF) offers promise as stress and strain sensors in CF reinforced composite materials as well as for modifying and improving the fiber-matrix interface. However, there has been no research investigating electromechanical properties of CNT/CF, which is needed for sensor development. This work reports the results of simultaneous measurements of electrical and mechanical properties of individual CNT/CF during localized transverse compression experiments at very light loads ($\mu$N to mN) and small relative displacements (RDs) (nm to a few $\mu$ms). Although the present experiments are conducted with isolated CNT/CF structures (i.e., not within a composite), results are expected to have applicability to behavior in composites and serves as a starting point in enabling this technology.

Since CNT/CF structure is primarily associated with composite materials, some discussion of composite technology is included to provide insight into the problem. The majority of CF used today is made from polyacrylonitrile (PAN) precursor. PAN-based CFs generally exhibit higher tensile and compressive strength, higher strain to failure, and lower elastic modulus as compared to mesophase pitch-based CFs. The PAN fiber/matrix interface can be modified for improved mechanical, electrical, and thermal properties, e.g., for expanded use of such composite materials in aerospace vehicles. The interface between CFs and the resin matrix has a discontinuity in properties that often leads premature failure or inefficient transfer of electrical or thermal energy. CNTs have excellent mechanical, electrical, and thermal properties and offer a method to tailor the fiber-matrix interface. A fundamental understanding of the coupling between mechanical and electrical properties of CNT/CF is needed to maximize the usefulness of the materials as both fillers in composites and as stress and strain sensors for composite health monitoring. Methods to grow aligned CNTs on CF have been developed in past studies, and the resultant structures are utilized here as multicomponent fiber materials.[1–4]

Mechanical properties of individual CFs, CNTs, and

---

a)Author to whom correspondence should be addressed. Electronic mail: steve.patton@wpafb.af.mil.

    **106**, 104313-1     © 2009 American Institute of Physics

CNT/CFs have been investigated, and there are multiple reviews discussing the mechanics of CNTs and their bundles.[5,6] For compression and bending loads, elastic buckling of CNTs at a critical force was established as a prime deformation mechanism.[7–9] Both single-walled CNTs (SWCNTs) and multi-walled CNTs (MWCNTs) were shown to have remarkable bending flexibility up to a critical bending angle beyond which buckling occurs.[10] The bending and buckling behavior is fully reversible despite the occurrence of multiple kinks and highly strained tube regions.[10] The force versus strain dependence of CNT bundles was demonstrated to have nonlinear behavior at high strain.[11] In addition, their stiffness was found to be much higher in tension than in compression.[12] Mechanical properties of vertically aligned CNT forests and CNT-polymer nanocomposites were also investigated using nanoindentation.[13,14] In the case of vertically aligned CNT forests, nanotubes were consecutively bent during penetration of the indenter.[14] For vertically aligned CNT nanotube forests, kinking under compression was shown to produce a cooperative folding effect, which eventually led to a transition from low to a high stiffness at about 60%–70% strain.[15]

The literal analyses just given are mostly based on either axial (compressive or tensile) or bending loading of CFs and CNTs. Transverse mechanical properties of CF and CNTs have received considerably less attention than longitudinal properties.[16–19] Transverse properties are important with respect to complex loading at the fiber-matrix interface and thus warrant investigation. Force-displacement curves during radial compression of individual CNTs using atomic force microscopy (AFM) were reported to be linear at low strain but became nonlinear above 30% strain.[16,17] Due to the nonlinearity at high strain, the mechanical properties are strongly dependent on the mechanical loading direction and applied pressure. For example, transverse compressive elastic modulus of MWCNTs was measured with AFM with a range of values reported from 0.3 to 80 GPa.[16,17]

Anisotropic and strain dependent electrical properties of CNT assemblies offer possibility of their use as *in situ* sensors in composite materials. Electrical current flow in CNT ropes or mats involves metallic conduction and charge hopping or tunneling through electrical barriers associated with defects, with the degree of the metallic conductivity being strongly dependent on the tube multiwall or single-wall morphology, chirality, length, diameter, and surface chemical functionalization.[20–25] For the purpose of this study, the interest also encompassed the dependence of the electrical properties on the strain imposed on the CNT array. For example, when SWCNTs and MWCNTs were investigated for thin-film field-effect transistor (FET) applications,[26,27] structural deformation of MWCNTs (collapsed tubes) was found to be needed for MWCNTs to operate as FETs, illustrating a good coupling between mechanical deformation and electronic properties.[27–29] Electrical conductivity through CNT based materials is strongly influenced by the establishment of good tube-tube electrical interfaces. For example, electrical conductivity of a CNT block increased with increased compressive strain, and reversible behavior was attributed to elastic bending of CNTs.[30] Contact resistance between CNT coated electrodes in direct contact was found to be lower in air than in vacuum illustrating environmental sensitivity of such interfaces.[31] SWCNT and MWCNT films were studied for possible use as stress and strain sensors.[32,33]

The previously mentioned studies have demonstrated the potential of CNTs to detect compressive load through tube electrical property monitoring and the importance of both mechanical properties and chemical surface state. However, there have been no such investigations for CNTs attached on CF surfaces, which is of prime interest for their use as sensors in CF reinforced composites. Investigations of CNT/CF with electrical-mechanical correlations under controlled loads and environments are needed to develop quantifiable stress sensing techniques.

The objective of this investigation was to determine the electromechanical response of CNT/CF during micro/nanoscale compression experiments. Very light loads ($\mu$N to mN) and small RDs (nm to a few $\mu$ms) during compression experiments differentiates this work from many of the previous studies that used higher loads and higher displacements. This allows us to better understand the use of these materials to sense small displacements. This paper discusses the results of experiments that investigate the coupling of electrical and mechanical behavior of CNT/CF under localized transverse compression and compares the behavior with CF alone. The results are interpreted in light of known deformation and conduction mechanisms of CF and CNTs and extrapolated to possible sensor applications in composite materials. Results here may differ from behavior of CNT/CF within a polymer composite material (where the in between spaces of CNT forest are filled with an insulator), but the present study serves as a basis for development of this technology.

## II. EXPERIMENTAL

A micro/nanocontact apparatus was used for this study and is shown schematically in Fig. 1(a). The apparatus has been described in detail in earlier studies that investigated adhesion of microelectromechanical systems (MEMS) materials and performance of MEMS rf switch contacts.[34–40] A ball-on-flat electrode configuration is used with Au-coated GaAs wafers and Au-coated 1.6 mm diameter grade 100 440 C stainless steel balls. Deposition techniques and properties of the Au films were described in detail in an earlier publication.[35] The root mean square roughnesses of the Au-coated wafers and balls were 17.6 and 13.6 nm, respectively.[35] The fiber was sandwiched between the electrodes in radial compression experiments as shown in Fig. 1(b). The apparatus is capable of measuring force with $\mu$N-scale resolution and displacement with nm-scale resolution. In this study, peak forces used were generally of the order of 1 mN and peak displacements of the order of a few micrometers. The micro/nanocontact apparatus was placed inside an environmental chamber, which was purged with dry nitrogen to a relative humidity (RH) of less than 1%. The chamber was vented to maintain atmospheric pressure. A thermohygrometer was used to monitor the temperature and RH inside the chamber. The temperature inside the chamber was $22 \pm 1$ °C during experiments. The ball, flat, and fiber
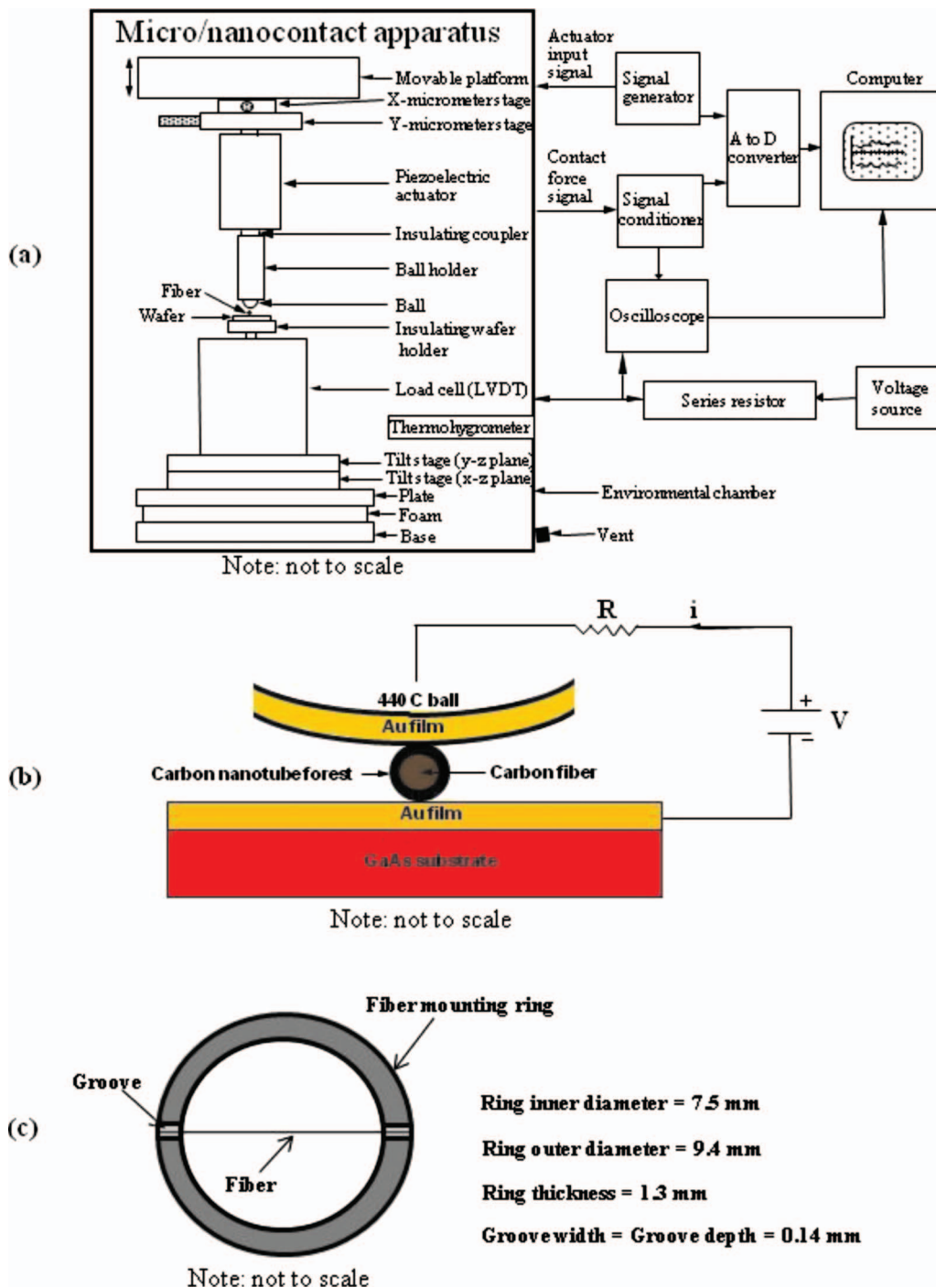
FIG. 1. (Color) (a) Schematic of the micro/nanocontact apparatus and associated instrumentation used in fiber indentation experiments. (b) Close up view of the ball-fiber-wafer contact along with the electric circuit used in this study. Fiber axis is into the page resulting in a localized radial compression of the fiber. (c) Schematic of the ring used for fiber mounting.

were maintained at the stated conditions for 1 h prior to experimentation to ensure thermal and environment purge equilibrium.

Figure 1(b) shows a close up view of the ball-fiber-wafer contact along with the electrical circuit used for electrical resistance measurements. Transverse compression experiments on CF and CNT/CF sandwiched between Au electrodes were conducted using a piezoelectric actuator for ball displacement. To position fiber samples between ball-flat gold electrodes, a special electrically insulating ring-shaped holder was designed and fabricated to hold fiber specimens

and is shown schematically in Fig. 1(c). The inner diameter of the ring is 7.5 mm, and the outer diameter is 9.4 mm. The thickness of the ring is 1.3 mm. Diametrically opposite channels with 0.14 mm width and 0.14 mm depth were milled onto the ring for mounting the fiber, which was secured in the channels with an adhesive. The fiber holder was then placed on the Au-coated wafer with the grooved fiber side facing down onto the wafer. This allowed the fiber to be supported by the flat gold surface. The movable platform with *x*- and *y*-micrometer stages [Fig. 1(a)] was used to position the ball directly above the fiber. The piezoelectric ac-

tuator was used to approach the ball to the fiber and control ball displacement in fiber radial compression experiments. The actuator was driven in a closed loop analog mode with a signal generator. A triangle wave excitation input signal was applied to the actuator, and a constant approach and retract ball speed of 1.28 $\mu$m/s was used in experiments unless otherwise noted. This controlled displacement of the ball electrode initiated fiber radial compression against the flat electrode, and the resulting compression force and displacement of the lower electrode were measured with the high sensitivity load/displacement cell shown in Fig. 1(a). A constant open circuit voltage of 1 V was used along with a fixed resistor of 100 k$\Omega$ assembled in series with gold plated electrodes to limit the current to less than 10 $\mu$A [Fig. 1(b)]. Voltage drop across the fiber was monitored with an oscilloscope and stored in a computer. Simple circuit analysis was used to calculate the sandwiched fiber electrical resistance. The maximum measurable electrical resistance with the circuit and instrumentation was $10^9$ $\Omega$. The above procedure was found to be a reliable way to conduct the experiments.

A PAN-based CF (T650-35 by Fabric Development, Inc.) was used in this study and has been widely used in aerospace fiber-reinforced composites. The material is commercially available in sized and unsized fibers. Sized fibers are typically coated with an epoxy surface treatment that is specifically formulated to enhance tensile and interface properties. Unsized fibers do not have this surface treatment. The T650-35 fiber used in this study is of the unsized variety. The fiber diameter was 7 $\mu$m. Typical transverse compressive elastic modulus of PAN-based CFs is about 10 GPa.[18,19]

The silica coated CF was fabricated in a high temperature furnace at 1100 °C with a flow mixture of Ar (300 ml/min) and $H_2$ (40 ml/min) carrying $SiCl_4$ for 20 min in the presence of a trace amount of $O_2$ under atmospheric pressure to form a <10 nm layer of $SiO_2$ on the CF to form a $SiO_2$/CF structure.[2] Aligned MWCNTs were then grown by chemical vapor deposition (CVD) on the $SiO_2$/CF by pyrolysis of FePc under Ar/$H_2$ atmosphere at 800–1100 °C according to the published procedure.[1,2] The resulting structure is referred to as CNT/$SiO_2$/CF in this paper. The length of CNTs was about 4 $\mu$m with diameters between 20 and 80 nm. The CNTs were aligned radially with the pretreatment of $SiO_2$ on the CF surface. The CNT density at the CF surface for similar CNT/$SiO_2$/CF was calculated to be 9.6 $\times 10^9$/cm$^2$ in an earlier publication.[4] CVD synthesis method was chosen because it can easily be scaled up and allows uniform MWCNT array growth on surfaces with complex geometry and is compatible with PAN fiber material. Figure 2 shows a cross-sectional schematic and a SEM image of the resulting CNT/$SiO_2$/CF structure. The diameter of the structure is about 15 $\mu$m (7 $\mu$m CF core and 8 $\mu$m MWCNTs) as shown in Fig. 2(a). Figure 2(b) shows a radial view of the fiber showing the nanotube forest on the outside of the CNT/$SiO_2$/CF.

## III. RESULTS AND DISCUSSIONS

Results of fiber compressions for (a) CF and (b) $SiO_2$/CF are shown in Fig. 3. Force and resistance are plot-
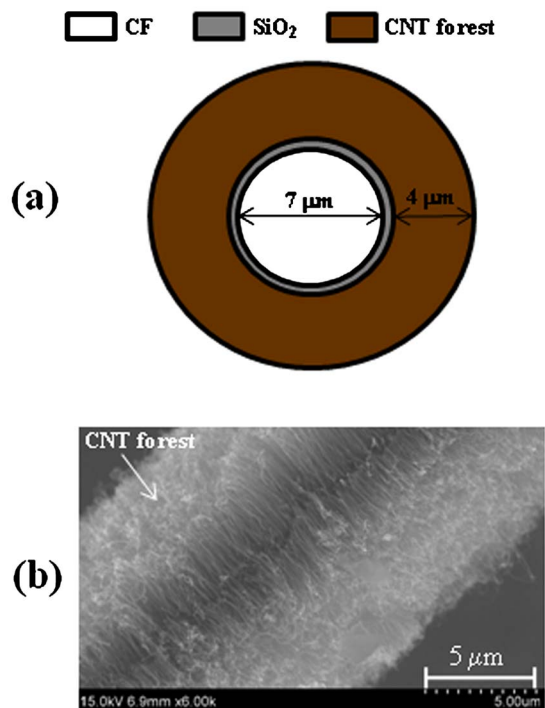
FIG. 2. (Color online) Schematic (a) and SEM micrograph (b) of the CF-oxide-CNT structure used in compression experiments where (b) is a radial view.
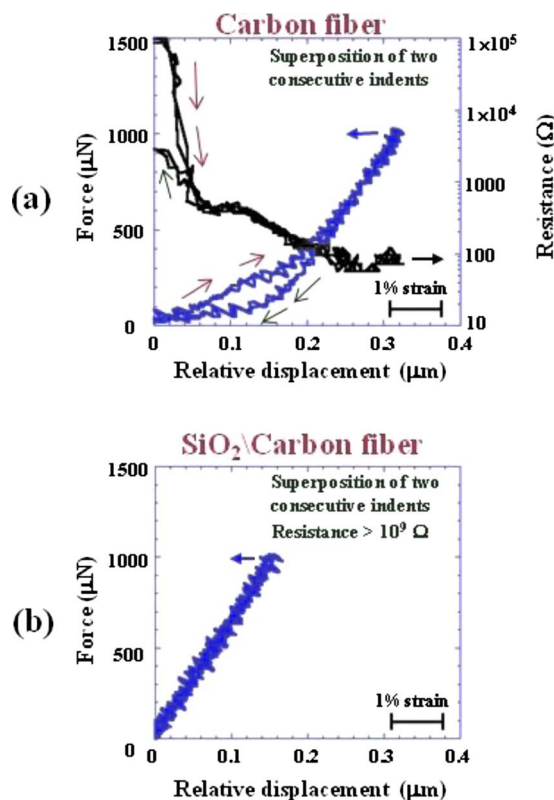
FIG. 3. (Color online) Force and resistance versus RD curves for (a) CF and (b) $SiO_2$/CF during localized radial compression experiments. For the CF, force increased and resistance decreased as strain increased with some hysteretic behavior in both force and resistance at low strain. Note the logarithmic scale for resistance. $SiO_2$/CF showed high resistance, negligible electrical conduction, and a linear force-displacement curve.

ted as a function of relative displacement (RD). RD is the compressive displacement or penetration imposed on the fiber specimens at the ball apex. The relationship between RD and strain on the fiber specimen at the ball apex ($\varepsilon$) is

$$\varepsilon = RD/w, \tag{1}$$

where w is the width of the fiber specimen. A strain scale bar is given in Figs. 3(a) and 3(b) based on w=7 $\mu$m for the CF and $SiO_2/CF$. Both compression and decompression data are shown. The peak force in each experiment is about 1000 $\mu$N. Each graph is the superposition of data from two consecutive indentation cycles (one cycle=compression then decompression) and illustrates the excellent repeatability of the data. Figure 3 shows distinct differences in behavior for the CF and $SiO_2/CF$ samples during compression experiments.

Force increased with RD for the CF sample in Fig. 3(a). There is some nonlinearity and hysteresis in the first 200 nm of RD. The peak force of 1000 $\mu$N is attained at about 320 nm of RD (4.6% compressive strain). The CF radial compression stiffness was calculated from the slope of the unloading force-displacement curve near peak load and is about 5560 N/m. Although surface roughness of the Au ball prevented determination of elastic modulus through Hertzian analysis, some analysis was conducted assuming smooth surfaces for the ball-on-fiber contact. Transverse elastic modulus for the CF was calculated using data from Fig. 3(a) and

$$E' = \frac{W}{\pi \bar{k}} \left( \frac{4.5}{\delta^3} \frac{\bar{\xi}^3}{\bar{\varepsilon}} \frac{1}{R'} \right)^{0.5}, \tag{2}$$

where $E'$ is the reduced Young's modulus, $W$ is the load, $\bar{\xi}$ and $\bar{\varepsilon}$ are simplified elliptic integrals, $\bar{k}$ is the ellipticity parameter, $\delta$ is the maximum deflection, and $R'$ is the reduced radius of curvature.[41] Assuming smooth surfaces allows the calculation of a lower bound for the elastic modulus of the fiber since the real area of contact (RAC) is less than the apparent area of contact. The calculated transverse elastic modulus for the CF using Eq. (2) is 0.59 GPa. In this calculation, the elastic modulus and Poisson's ratio used for Au were 79 GPa and 0.42, respectively. Poisson's ratio used for the PAN-based CF was 0.3.[19] The calculated value (0.59 GPa) is less than the literature value for the transverse compressive elastic modulus of PAN-based CF of about 10 GPa.[18,19] The discrepancy is due to surface roughness of the fiber and Au specimens. The RAC for rough surface contacts is typically a few percent of the nominal contact area.[42,43] The ratio of the calculated transverse elastic modulus for the CF (0.59 GPa) to the literature value (10 GPa) is 0.059, which suggests a reasonable RAC of 5.9% of the nominal contact area.[42,43]

The Hertzian contact area for smooth contacts was calculated to be $4.79 \times 10^{-11}$ m$^2$ (ellipse semiminor axis =0.68 $\mu$m across the fiber and semimajor axis=22.3 $\mu$m along the fiber). RAC was calculated to be $2.82 \times 10^{-12}$ m$^2$ using 5.9% as the percentage RAC of the nominal area. For comparison, pure plastic RAC was calculated to be 1.47 $\times 10^{-12}$ m$^2$ using

$$RAC = W/H, \tag{3}$$

where $H$ is the hardness of Au (0.676 GPa). The contact area calculations are self-consistent with the rough surface elastic RAC being smaller than the Hertzian area and larger than the pure plastic RAC. Although the preceding contact analysis is useful, no additional contact analysis of $SiO_2/CF$ and $CNT/SiO_2/CF$ specimens will be pursued in this paper due to further structural complexity. Contact stiffness is provided for each of CF, $SiO_2/CF$, and $CNT/SiO_2/CF$ in this paper and provides a useful comparison of mechanical properties.

Electrical resistance decreased with increasing compressive force in Fig. 3(a), reaching values less than 100 $\Omega$ at 400 $\mu$N force and above. The decrease in resistance is consistent with an increase in the RAC at high force. There is resistance hysteresis at low RD with resistance being lower during decompression as indicated by the compression and decompression arrows. Lower resistance is consistent with higher RAC during decompression. Since consecutive indentation curves coincide in Fig. 3(a), plastic deformation was not the origin of the observed hysteresis. Hysteresis in force-displacement curves and contact area is known to occur in elastic contacts with lower force and higher contact area during unloading as compared to loading.[44,45] Elastic deformation of surface asperities on the CF surface is a plausible explanation of the hysteresis in force and resistance in Fig. 3(a). Asperity deformation is thought to play a key role since hysteresis is present at small RD with force and contact area (resistance) trends being consistent with elastic contact behavior.[44,45]

The $SiO_2/CF$ sample in Fig. 3(b) shows a more rapid increase in force as compared to the unmodified CF. Electrical resistance data are not shown because it was greater than $10^9$ $\Omega$, which is the highest measurable resistance with the measurement system and instrumentation. A linear force-displacement curve and no hysteresis are likely due to stiffening of asperities on the CF surface from the oxide coating. This hypothesis is supported by the fact that hysteretic behavior in elastic contacts decreases with less deformable high elastic modulus materials.[44,45] Low conductivity for the oxide coating is expected since the $SiO_2$ coating is an electrical insulator. An electric field strength of 1430 V/cm was established under compression based on the $SiO_2/CF$ diameter and open circuit voltage, which is about four orders of magnitude below the $SiO_2$ dielectric breakdown field strength. It has been suggested that the thin nature of the oxide (<10 nm) and/or the possible presence of pinholes could ensure effective charge transport through the contact.[2] However, data presented here suggests that such conduction did not occur. The absence of electrical response for $SiO_2/CF$ means that is not useful for sensor applications. Peak force of 1000 $\mu$N was attained at a small RD of 150 nm (2.1% compressive strain). Stiffness of the $SiO_2/CF$ is about 6250 N/m and is slightly higher than that observed for the CF, which is reasonable to expect due to a small mechanical property contribution from the thin $SiO_2$ shell to the CF core properties.

Results of fiber compressions for $CNT/SiO_2/CF$ are shown in Fig. 4. Compression experiments were performed at various peak RD while measuring force and resistance.

CNT/SiO$_2$/CF



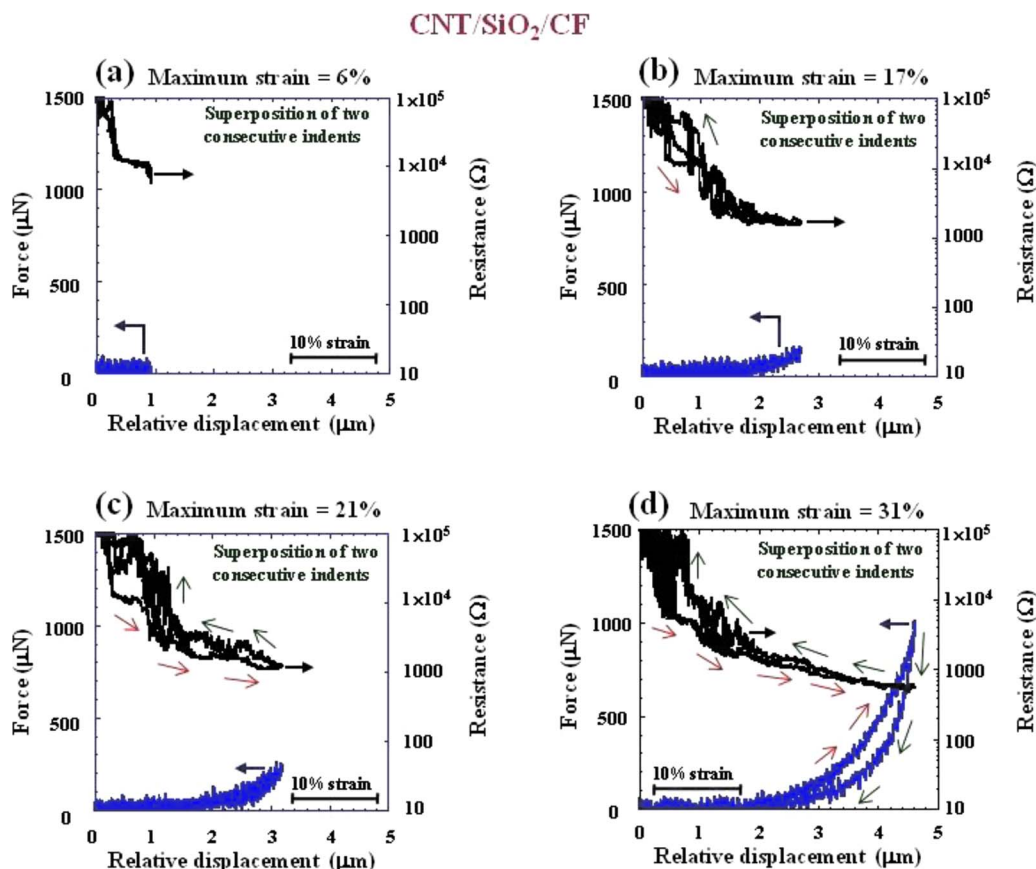FIG. 4. (Color online) Force and resistance versus RD curves for CNT/SiO$_2$/CF at various peak RDs: (a) 0.9 $\mu$m (6% strain), (b) 2.6 $\mu$m (17% strain), (c) 3.2 $\mu$m (21.3% strain), and (d) 4.6 $\mu$m (31% strain). Force hysteresis is evident only at high maximum strain in (d). Resistance hysteresis is evident at 17% maximum strain and above [(b)–(d)] and is most obvious at low RD. Note the logarithmic scale for resistance.

Figure 4 investigates the effect of maximum strain on electromechanical properties. A strain scale bar is given in Figs. 4(a)–4(d) based on w=15 $\mu$m (diameter of CNT/SiO$_2$/CF) in Eq. (1). However, most of the deformation likely occurred in the CNTs themselves due to the compliance of the CNT forest. Thus, the 8 $\mu$m diameter of the CNT forest could be used as w in Eq. (1) to more accurately define strain on the CNTs. The reader should keep in mind that the actual CNT strain is about twice the value of the composite fiber structure calculated with w=15 $\mu$m. Peak RD was 0.9 $\mu$m (6% strain) in Fig. 4(a), 2.6 $\mu$m (17% strain) in Fig. 4(b), 3.2 $\mu$m (21% strain) in Fig. 4(c), and 4.6 $\mu$m (31% strain) in Fig. 4(d). Measurable electrical conduction occurred for CNT/SiO$_2$/CF. Since electrical conduction was negligible for the SiO$_2$/CF sample, the process of depositing CNTs on the SiO$_2$/CF sample is assumed to result in a conductive path from CNTs through the oxide to the CF. It was suggested earlier that the thin nature of the SiO$_2$ coating could allow electron tunneling between the CNTs and underlying CF.[2] Electron tunneling has been observed across an insulating monolayer between SWCNTs and a Au substrate.[46] Severe distortion of the thin SiO$_2$ layer during CNT growth was reported earlier, where it was suggested that penetration of the tubes through the oxide would facilitate electrical and thermal conduction.[2] The results reported here support such a hypothesis.

At a peak RD of 0.9 $\mu$m (6% strain) in Fig. 4(a), no hysteresis is evident in either force (remains zero throughout) or resistance. Resistance dropped rapidly over the first half micron of RD but decreased at a lower rate from 0.5–1 $\mu$m RD. When the peak RD was increased to about 2.6 $\mu$m (17% strain) in Fig. 4(b), no force hysteresis was observed, but resistance hysteresis was evident. Resistance decreased as RD increased, and resistance was lower during compression than during decompression as indicated by the arrows in Fig. 4(b). Force began to increase at RDs above about 2 $\mu$m (13% strain). Figure 4(c) shows the result for 3.2 $\mu$m peak RD (21% strain). The result is similar to Fig. 4(b) except for higher peak force and lower resistance at the corresponding peak RD. Figure 4(d) shows the result for 4.6 $\mu$m peak RD (31% strain) and shows force hysteresis that was not observed in the other cases. Highest peak force and lowest resistance at peak displacement are also observed in Fig. 4(d).

Figure 4 shows that significant force hysteresis occurred only at the highest peak RD (31% strain) in Fig. 4(d). Hysteresis of loading-unloading compressive stress versus strain was reported before for MWCNT forests as in Fig. 4(d),[15] indicating that our data support the generally observed mechanical behavior of aligned and vertically compressed MWCNTs. It was suggested that internal friction is the energy loss mechanism for compressed MWCNTs.[20] Energy loss due to internal friction was found to be dependent on strain amplitude for a wide variety of solids.[47] This is con-

sistent with the results in this paper and is intuitive since higher sliding distances between entangled nanotubes per compression-decompression cycle are expected at high maximum strain. Stiffness was calculated to be about 100 N/m in Fig. 4(b), 250 N/m in Fig. 4(c), and 3300 N/m (~1/2 CF stiffness) in Fig. 4(d), which illustrate that stiffness increased at higher maximum RD. These results are consistent with a previous study where force-displacement curves during nanoindentation of vertically aligned CNT forests were nonlinear with increasing slope at higher displacement (~50 N/m stiffness at ~50% CNT compressive strain).[13] Moreover, previous studies of flat MWCNT forest surfaces under compression showed a transition from compliant to stiff behavior at about 65% strain, which was explained by nanotube folding leading to less compliance.[15] However, we observed the compliant-stiff transition of $CNT/SiO_2/CF$ at smaller strain (~30%). This may be due to the fact that we used w=15 $\mu$m in Eq. (1), which may underestimate strain of the compliant CNT forest. The actual strain on CNTs is about 60% in this study if it is considered that most of the deformation takes place at CNTs [compare peak RD at 1000 $\mu$N force in Figs. 3(a) and 3(b) with Fig. 4(d)], which is more consistent with the previous work.[15]

Hysteresis in resistance shown in Figs. 4(b)–4(d) is perhaps a novel result. Resistance hysteresis is evident at maximum strains as low as 17% [Fig. 4(b)]. The equivalent resistance ($R_{eq}$) of N identical resistors in parallel is

$$R_{eq} = R/N, \qquad (4)$$

where $R$ is the resistance of a single CNT. The $1/N$ dependence of $R_{eq}$ explains the more readily apparent resistance hysteresis at low RD in Figs. 4(b)–4(d) since $N$ is small at low strain.

The effect of strain rate on force and resistance hysteresis was investigated, and the results are shown in Fig. 5. Strain rate was varied by varying ball speed during compression experiments. Maximum strain rate was $8.53 \times 10^{-4}$ s$^{-1}$ in Fig. 5(a) and $8.53 \times 10^{-3}$ s$^{-1}$ in Fig. 5(b). There are no significant differences in hysteresis behavior of either force or resistance at different strain rates in Figs. 5(a) and 5(b). Data in Fig. 5 are directly comparable to Fig. 4(d) (maximum strain rate=$8.53 \times 10^{-2}$ s$^{-1}$). There is no difference in the data presented in Figs. 5 and 4(d), which indicates that force and resistance behavior does not depend on strain rate over the range of strain rates tested in this study. Energy loss due to internal friction was found to be independent of strain velocity for a wide variety of solids.[47] This is consistent with the observations in this study.

Resistance versus force for CF and $CNT/SiO_2/CF$ is shown in Fig. 6. Data in Fig. 6 are of interest for use of the fibers as force and stress sensors in future smart composites. Hysteresis is evident for the CF in Fig. 6(a) with lower resistance during decompression. This is consistent with the previous discussion of Fig. 3(a). Hysteresis is problematic from a sensor point of view since a particular resistance value may represent two different force or pressure values. The hysteresis problem is not present to the same degree for the $CNT/SiO_2/CF$ in Fig. 6(b), which is an advantage over the CF for force and stress sensing applications. Data in
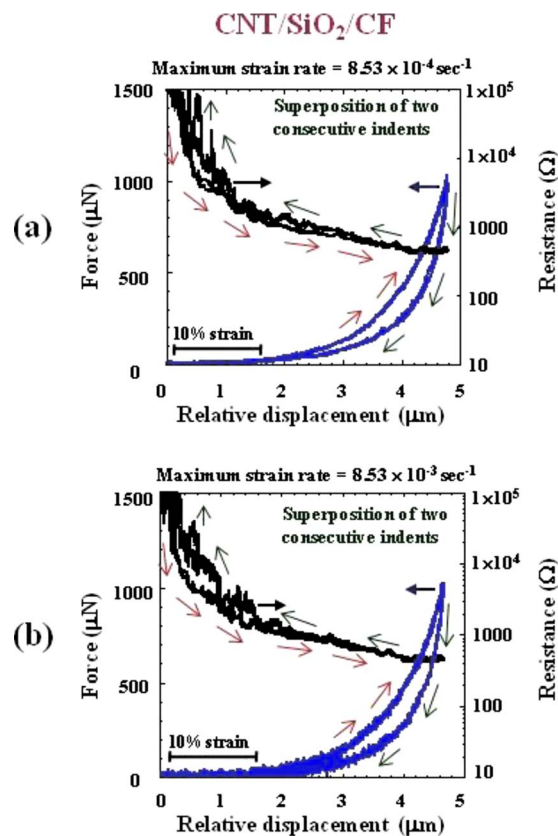


FIG. 5. (Color online) Force and resistance versus RD for $CNT/SiO_2/CF$ at a maximum strain rate of (a) $8.53 \times 10^{-4}$ s$^{-1}$ and (b) $8.53 \times 10^{-3}$ s$^{-1}$. Force and resistance hysteresis did not depend on strain rate over the range tested in this study. Note the logarithmic scale for resistance.
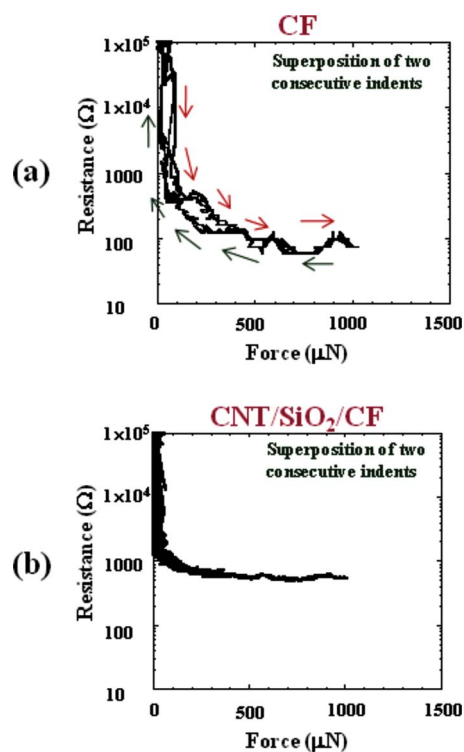


FIG. 6. (Color online) Resistance versus force for (a) CF and (b) $CNT/SiO_2/CF$. Note the logarithmic scale for resistance.
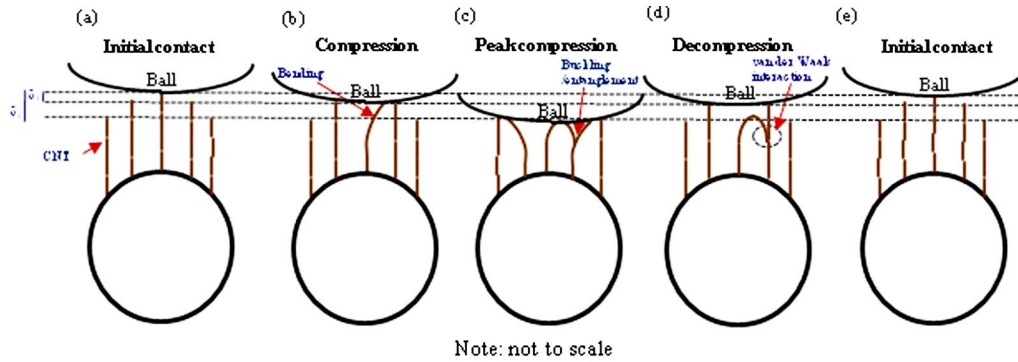
FIG. 7. (Color online) Simplified schematic of CNT deformation during compression-decompression experiments. Bending and buckling of nanotubes during compression led to entanglement and internal friction. Van der Waals force hindered disentanglement during decompression and reduced the number of current paths leading to higher resistance.

Fig. 6(b) are also smoother than data in Fig. 6(a) due to the multiple individual contacts for the $CNT/SiO_2/CF$ as opposed to a larger contact area for the CF.

Figure 7 shows a simplified schematic of CNT deformation during compression-decompression experiments. Primary deformation mechanisms for nanotubes subject to compressive force are axial compression, bending, and buckling. The two general deformation sequences are axial compression then buckling or bending then buckling. Figure 7 illustrates that the bending-buckling hypothesis that is most likely for the curved geometry in our experiments. Figure 7(a) shows the initial contact with the center (highest) CNT. In Fig. 7(b), the ball has compressed the CNT forest by a distance of $\delta_1$ to contact the two CNTs adjacent to the center CNT that is now bent. Further compression of the CNT forest to a distance $\delta_2$ brings the ball into contact with the lowest nanotubes and is depicted in Fig. 7(c). The center nanotube has now buckled into contact with its nearest neighbor and has experienced tangling and internal friction. This is the origin of hysteretic energy loss that is apparent in Fig. 4(d) at a maximum strain of 31%. The two CNTs adjacent to the center CNT are now bent. The ball is then retracted (decompression) back to a compression distance of $\delta_1$ for the CNT forest as shown in Fig. 7(d). However, the van der Waals force between the center CNT and its nearest neighbor does not allow the longest nanotube to move. CNTs with diameters over 25 Å were found to flatten against each other under van der Waals attraction.[48] This supports the mechanism being put forward in this paper. The CNT forest has a different configuration at a compressive distance of $\delta_1$ during compression [Fig. 7(b)] and decompression [Fig. 7(d)]. It is hypothesized that this is the origin of resistance hysteresis.

There are three CNT electric current paths bridging the contact in Fig. 7(b) but only two in Fig. 7(d). Resistance will be less in Fig. 7(b) than in Fig. 7(d) by Eq. (4) and as shown in Fig. 4. It is unlikely that the observed resistance hysteresis effects are due to different resistivity of the CNTs originating from electromechanical effects[27–29] since the strain on the CNT forest is the same in Figs. 7(b) and 7(d). Finally, in Fig. 7(e) the CNT forest returns to its original configuration as the ball is retracted to its original position. The center nanotube returns to its original position in going from Figs. 7(d) and

7(e) once its nearest neighbor loses contact with the ball and its rigidity associated with bending or compressive strain. Due to the weak van der Waals interaction, a free standing tube cannot constrain its nearest neighbor to a compressed (buckled) configuration once the contact is fully unloaded, which completes the contact decompression cycle.

The authors would like to address the applicability of our results to sensing applications in composite materials. The results are fully applicable for using CF and $CNT/SiO_2/CF$ as stand-alone stress and strain sensors. In the case of CF, the results are applicable to CF reinforced composite materials. However, in the case of $CNT/SiO_2/CF$, the space between the CNTs is filled with a reinforcing polymer insulator that changes the deformation mechanics as well as reduces the number of CNT-CNT contacts. Thus, smaller changes in resistance for a similarly applied load would be expected due to less deformation of the CNT-polymer composite and a smaller change in the number of CNT-CNT contacts. It should also be pointed out that the observed hysteresis behavior in force and contact resistance for $CNT/SiO_2/CF$ may be different for the CNT-polymer composite due to the difference in deformation and CNT contact mechanics as well as the viscoelastic effects of the polymer.

Although fracture strains in traditional composite materials are of the order of 1%–2%,[49,50] strain in CF reinforced shape memory polymer composites (CFSMPCs) can be as high as 150%.[49,51,52] Thus, results shown in this paper may have more applicability to higher strain applications such as CFSMPC.

## IV. SUMMARY

Electromechanical behavior of CF, $SiO_2/CF$, and $CNT/SiO_2/CF$ was investigated during localized radial compression at ultralow load and displacement. For CF, resistance decreased as force and strain increased, and hysteresis in both force and resistance was observed at low strain. $SiO_2/CF$ showed high resistance and negligible electrical conduction, and force-displacement curves were linear due to the presence of the thin oxide coating. $CNT/SiO_2/CF$ stiffness increased as force and strain increased and became comparable to that of CFs at high strain (~30%). Hysteresis

in both force-displacement and resistance-displacement curves was observed with CNT/SiO$_2$/CF but was more evident as maximum strain increased and did not depend on strain rate. Hysteretic energy loss is associated with internal friction between entangled CNTs. Van der Waals forces between deformed and entangled CNTs hindered disentanglement, which reduced the number of current paths and increased resistance during decompression. The results of this study provide new understanding of the mechanical and electrical behavior of CNT coated CF and will facilitate usage as stress and strain sensors in both stand-alone and composite material applications.

## ACKNOWLEDGMENTS

[1] S. Huang, L. Dai, and A. W. H. Mau, J. Phys. Chem. **103**, 4223 (1999).
[2] L. Qu, Y. Zhao, and L. Dai, Small **2**, 1052 (2006).
[3] L. H. Chen, J. F. AuBuchon, I. C. Chen, C. Daraio, X. R. Ye, A. Gapin, S. Jin, and C. M. Wang, Appl. Phys. Lett. **88**, 033103 (2006).
[4] Q. Zhang, J. Liu, R. Sager, L. Dai, and J. Baur, Compos. Sci. Technol. **69**, 594 (2009).
[5] D. Qian, G. J. Wagner, W. K. Liu, M. F. Yu, and R. S. Ruoff, Appl. Mech. Rev. **55**, 495 (2002).
[6] M. F. Yu, J. Eng. Mater. Technol. **126**, 271 (2004).
[7] B. I. Yakobson, C. J. Brabec, and J. Bernholc, Phys. Rev. Lett. **76**, 2511 (1996).
[8] C. Li and T. Chou, Mech. Mater. **36**, 1047 (2004).
[9] K. Jensen, W. Mickelson, A. Kis, and A. Zettl, Phys. Rev. B **76**, 195436 (2007).
[10] S. Iijima, C. Brabec, A. Maiti, and J. Bernholc, J. Chem. Phys. **104**, 2089 (1996).
[11] T. Xiao, Y. Ren, P. Wu, and K. Liao, Appl. Phys. Lett. **89**, 033116 (2006).
[12] C. P. Deck, J. Flowers, G. S. B. McKee, and K. Vecchio, J. Appl. Phys. **101**, 023512 (2007).
[13] H. J. Qi, K. B. K. Teo, K. K. S. Lau, M. C. Boyce, W. I. Milne, J. Robertson, and K. K. Gleason, J. Mech. Phys. Solids **51**, 2213 (2003).
[14] E. J. Garcia, A. J. Hart, B. L. Wardle, and A. H. Slocum, Adv. Mater. (Weinheim, Ger.) **19**, 2151 (2007).
[15] A. Cao, P. L. Dickrell, W. G. Sawyer, M. N. Ghasemi-Nejhad, and P. M. Ajayan, Science **310**, 1307 (2005).
[16] W. Shen, B. Jiang, B. S. Han, and S. Xie, Phys. Rev. Lett. **84**, 3634 (2000).
[17] M. F. Yu, T. Kowalewski, and R. S. Ruoff, Phys. Rev. Lett. **85**, 1456 (2000).
[18] H. Miyagawa, C. Sato, T. Mase, E. Drown, L. T. Drzal, and K. Ikegami, Mater. Sci. Eng., A **412**, 88 (2005).
[19] H. Miyagawa, T. Mase, C. Sato, E. Drown, L. T. Drzal, and K. Ikegami, Carbon **44**, 2002 (2006).
[20] A. B. Kaiser, Y. W. Park, G. T. Kim, E. S. Choi, G. Dusberg, and S. Roth, Synth. Met. **103**, 2547 (1999).
[21] A. B. Kaiser, K. J. Challis, G. C. McIntosh, G. T. Kim, H. Y. Yu, J. G. Park, S. H. Jhang, and Y. W. Park, Curr. Appl. Phys. **2**, 163 (2002).
[22] D. Hecht, L. Hu, and G. Gruner, Appl. Phys. Lett. **89**, 133112 (2006).
[23] E. Bekyarova, M. E. Itkis, N. Cabrera, B. Zhao, A. Yu, J. Gao, and R. C. Hadden, J. Am. Chem. Soc. **127**, 5990 (2005).
[24] D. Tasis, N. Tagmatarchis, A. Bianco, and M. Prato, Chem. Rev. (Washington, D.C.) **106**, 1105 (2006).
[25] R. Jin, Z. X. Zhou, D. Mandrus, I. N. Ivanov, G. Eres, J. Y. Howe, A. A. Puretzky, and D. B. Geohegan, Physica B **388**, 326 (2007).
[26] E. S. Snow, J. P. Novak, P. M. Campbell, and D. Park, Appl. Phys. Lett. **82**, 2145 (2003).
[27] R. Martel, T. Schmidt, H. R. Shea, T. Hertel, and Ph. Avouris, Appl. Phys. Lett. **73**, 2447 (1998).
[28] C. J. Park, Y. H. Kim, and K. J. Chang, Phys. Rev. B **60**, 10656 (1999).
[29] P. E. Lammert, P. Zhang, and V. H. Crespi, Phys. Rev. Lett. **84**, 2453 (2000).
[30] V. L. Pushparaj, L. Ci, S. Sreekala, A. Kumar, S. Kesapragada, D. Gall, O. Nalamasu, A. M. Pulickel, and J. Suhr, Appl. Phys. Lett. **91**, 153116 (2007).
[31] Y. Tzeng, Y. Chen, and C. Liu, Diamond Relat. Mater. **12**, 774 (2003).
[32] A. H. Barber, Q. Zhao, H. D. Wagner, and C. A. Baillie, Compos. Sci. Technol. **64**, 1915 (2004).
[33] X. Li, C. Levy, and L. Elaadil, Nanotechnology **19**, 045501 (2008).
[34] S. T. Patton, K. C. Eapen, and J. S. Zabinski, Tribol. Int. **34**, 481 (2001).
[35] S. T. Patton and J. S. Zabinski, Tribol. Lett. **18**, 215 (2005).
[36] S. T. Patton and J. S. Zabinski, Tribol. Lett. **19**, 265 (2005).
[37] S. T. Patton and J. S. Zabinski, J. Appl. Phys. **99**, 094910 (2006).
[38] S. T. Patton, K. C. Eapen, J. S. Zabinski, J. H. Sanders, and A. A. Voevodin, J. Appl. Phys. **102**, 024903 (2007).
[39] S. T. Patton, A. A. Voevodin, R. A. Vaia, M. Pender, S. J. Diamanti, and B. Phillips, J. Microelectromech. Syst. **17**, 741 (2008).
[40] S. T. Patton, J. M. Slocik, A. Campbell, J. Hu, R. R. Naik, and A. A. Voevodin, Nanotechnology **19**, 405705 (2008).
[41] G. W. Stachowiak and A. W. Batchelor, *Engineering Tribology* (Elsevier Butterworth-Heinemann, Burlington, MA, 2005), p. 307.
[42] M. Bahrami, M. M. Yovanovich, and J. R. Culham, Int. J. Heat Mass Transfer **48**, 3284 (2005).
[43] M. Zou, B. Yu, J. Cai, and P. Xu, ASME Trans. J. Heat Transfer **130**, 101301 (2008).
[44] P. Attard and J. L. Parker, Phys. Rev. A **46**, 7959 (1992).
[45] P. Attard, J. Phys. Chem. B **104**, 10635 (2000).
[46] P. Diao and Z. Liu, J. Phys. Chem. B **109**, 20906 (2005).
[47] A. L. Kimball and D. E. Lovell, Phys. Rev. **30**, 948 (1927).
[48] J. Tersoff and R. S. Ruoff, Phys. Rev. Lett. **73**, 676 (1994).
[49] K. Gall, M. Mikulas, N. A. Munshi, F. Beavers, and M. Tupper, J. Intell. Mater. Syst. Struct. **11**, 877 (2000).
[50] I. M. Daniel and O. Ishai, *Engineering Mechanics of Composite Materials* (Oxford, New York, 2006), p. 377.
[51] C. S. Zhang and Q. Q. Ni, Compos. Struct. **78**, 153 (2007).
[52] X. Lan, Y. Liu, H. Lv, H. Wang, J. Leng, and S. Du, Smart Mater. Struct. **18**, 024002 (2009).